Materials and Sustainability
https://www.sciltp.com/journals/matsus

Review

Cu-Based Atomic Catalysts for the Electrochemical Hydrogenation of Nitrate to Ammonia

Hyeong Bin Park and Haneul Jin *

Department of Energy and Materials Engineering, Dongguk University, Seoul 04620, Republic of Korea
* Correspondence: hjin1@dongguk.edu

How To Cite: Park, H.B.; Jin, H. Cu-Based Atomic Catalysts for the Electrochemical Hydrogenation of Nitrate to Ammonia. *Materials and Sustainability* **2025**, *1*(4), 14. https://doi.org/10.53941/matsus.2025.100014

Received: 22 April 2025
Revised: 13 July 2025
Accepted: 26 August 2025
Published: 20 November 2025

Abstract: Ammonia is an essential industrial feedstock, but conventional synthesis processes, Haber-Bosch process, emit significant greenhouse gases. Electrochemical ammonia synthesis offers a promising alternative, enabling ammonia production without harmful pollutants. Recently, electrochemical nitrate reduction has attracted considerable attention for ammonia synthesis due to its high selectivity. Achieving efficient ammonia synthesis requires active and selective catalysts, and single-atom catalysts have shown great promise owing to their tunable chemical and geometric active sites. However, challenges remain, including the need to enhance active surface area and suppress competing hydrogen evolution reactions. This minireview summarizes recent advances in the design strategies of Cu-based single-atom catalysts, highlighting their advantages and performance in electrochemical nitrate reduction. Special emphasis is placed on the relationship between local composition/atomic structure and electrochemical nitrogen reduction performance by studying their local atomic coordination such as Cu-N_4, Cu-N_xO, CuM-N_x, and Cu embedded metal oxides. The review concludes by emphasizing the importance of further research to optimize Cu-based single-atom catalysts for efficient and sustainable ammonia production.

Keywords: single atom catalyst; nitrate reduction reaction; ammonia production; electrochemistry

1. Introduction

Ammonia (NH_3) is a key chemical in various fields, such as pharmaceuticals, fertilizers, and energy [1–3]. Specifically, NH_3 is a critical energy vector in the global energy transition and has garnered considerable attention as a promising low-carbon material, serving as an organic hydrogen carrier and carbon-zero fuel [4–8].

The Haber-Bosch process is an essential chemical process for producing the majority of synthetic NH_3 under high temperature and pressure (300–550 °C and 250 bar with Fe oxide catalysts) [9–11]. However, the need for identifying alternative means of low-carbon NH_3 production, such as electrochemical NH_3 production, has been increasing globally owing to substantial CO_2 production; 3% of global CO_2 emissions are released during the Haber-Bosch process [12–15].

Electrochemical NH_3 production using nitrogen (N_2) or nitrate (NO_3^-) is a promising method for synthesizing carbon-neutral NH_3. Following Sabatier's principle, the N_2 reduction reaction and the NO_3^- reduction reaction (NO_3RR) consist of similar elemental steps as follows: (1) reactant molecules are transported and bound to the catalyst surface, (2) electrons and protons are added for hydrogenation, and (3) NH_3 is released. N_2 is an inert molecule, requiring a high N≡N bond dissociation energy of 941 kJ mol^{-1} and possessing extremely low solubility in aqueous electrolytes [1,12,13]. These limit the development of highly selective electrochemical systems providing large NH_3 yields. However, NO_3^- has garnered significant attention in the green NH_3 production stream owing to high solubility in water and selectivity for producing NH_3 [16,17]. Moreover, recent studies have

integrated electrochemical cells, coupling NO_x reduction at cathodes and concurrently producing NH_3 and value-added organics [18,19]. One of the principal factors determining the efficiency of electrochemical NO_3^- reduction is the choice of electrocatalyst. A variety of transition metal-based catalysts including those incorporating Fe, Cu, Ni, Co, Mo, or Pd, have been developed and have demonstrated promising performances in NO_3RR [20–22]. Among them, Cu-based single-atom catalysts (Cu-SACs) with tunable and isolated active centers have garnered considerable attention, owing to the similarity between the LUMO π* orbitals of NO_3^- and Cu, which can facilitate favorable orbital coupling [23,24].

This mini-review discusses recent advances of Cu-SAC for efficient NO_3RR, with a focus on the relationship between local atomic/electronic structures electrochemical performances. First, the fundamentals of electrochemical NO_3RR and the challenges associated with current electrocatalysts are introduced. Subsequently, strategies for the design of Cu-SACs are categorized according to the local coordination environment of the central Cu atom, including single-atom Cu coordinated by four N atoms (Cu-N_4), desymmetrized single-atom sites (Cu-N_xO/S), multi-element single-atom sites (CuM-N), and Cu embedded in metal oxides. Finally, future research directions are proposed to ensure efficient NO_3RR and advance practical NH_3 production systems.

2. Brief Understanding of the NO_3RR and the Associated Challenges

The electrochemical NO_3RR consumes eight electrons and nine protons to produce NH_3 at an equilibrium potential (E^0) of 0.7 V_{RHE} [25].

$$NO_3^- + 9H^+ + 8e^- \rightarrow NH_3 + 3H_2O$$

Conversion of NO_3^- involves three critical processes as follows: (1) adsorption of NO_3^- on the catalyst surface (activation), (2) deoxygenation and hydrogenation of $*NO_3^-$ (catalytic reaction), and (3) desorption of $*NH_3$ from the catalyst surface (recovery) [26,27]. At the beginning of the reaction, NO_3^- is adsorbed on the catalytic center, and the first deoxygenation step occurs via water dissociation ($*NO_3 + H_2O \rightarrow *NO_2 + 2OH^-$). After several deoxygenation steps of the $*NO_3^-$, two major routes emerge for the formation of NH_3 from the *NO intermediate. These include hydrogenation pathway ($*NO \rightarrow *HNO \rightarrow *H_2NO \rightarrow *NH_2OH \rightarrow *NH_3 \rightarrow NH_3(g)$ (route 1), and deoxygenation and hydrogenation pathway ($*NO \rightarrow *N \rightarrow *NH \rightarrow *NH_2 \rightarrow *NH_3 \rightarrow NH_3(g)$ (route 2). In route 1, *NO is sequentially hydrogenated to form $*NH_3$ over several steps, whereas in route 2, *NO is first deoxygenated to *N, followed by sequential hydrogenation to produce $*NH_3$. Theoretical studies have revealed that Cu(111) and Cu(100) surfaces possess high activation barriers for N* formation via NO* deoxygenation; therefore, route 1 is more favorable for the NO_3RR than route 2 [28]. While the NO_3^- reduction process is generally exothermic, the desorption of NH_3 is endothermic across all pH ranges, indicating that efficient NH_3 desorption from the catalyst surface is also crucial for high NO_3RR performance.

Although the E^0 of the NO_3RR is 0.7 V_{RHE}, previous studies have revealed that the range of applied potential varies between −1.5 V_{RHE} to −0.1 V_{RHE} depending on the pH of the electrolytes, owing to the large activation overpotential required to drive the NO_3RR [25]. In these potentials, a strong hydrogen evolution reaction (HER) occurs, which reduces Faraday efficiency (FE) and lost protons for the hydrogenation of NO_3^-. Figure 1C shows the difference between the limiting potentials of the NO_3RR and the HER using various metals, and a positive $U_L(NO_3RR)—U_L(HER)$ value indicates higher selectivity toward the NO_3RR than toward the HER [25]. Cu yields a positive value of $U_L(NO_3RR)—U_L(HER)$, whereas transition metals such as Co, Ni, Ru, Rh, Pt, Ir, and Pd yield negative values, indicating that Cu is the most selective element among various transition metals for NO_3RR over the HER.

Despite metallic Cu being the primary catalyst for NO_3RR, effective catalysts should possess suitable stereospecific geometric characteristics to optimize NO_3^- adsorption and the overall NO_3RR process. For example, the O-O distance in NO_3^- is 2.21 Å, and a Cu-Cu pair with an interatomic distance close to 2.21 Å can serve as an active center. However, controlling Cu-Cu distances on a Cu crystal is hardly achievable. Additionally, the Cu metal surface typically suffers from NO_2^- poisoning, which results in lowered NH_3 production rate [28,29]. These issues are primarily attributed to the weak binding between bulk Cu and intermediate species, as well as inadequate adsorption, deoxygenation, or proton transfer under operating condition. Cu-SACs, featuring electron-deficient $Cu^{\delta+}$ center, have emerged as promising alternatives. These catalysts demonstrate strong binding with intermediate species, thereby affording a high conversion rate and enhanced NH_3 selectivity [30].

Despite recent progress, the rate of NH_3 production on SACs remains constrained by linear scaling relationships, which stems from the challenge of using a single-active site for the multi proton/electron transfer NO_3RR process. To further improve the performance of Cu-SACs in NO_3RR, several issues must be overcome (Figure 1D). Typically, Cu-SACs are synthesized through thermal treatment of metal-carbon precipitates, such as metal-organic frameworks, however, this method does not allow for precise structural control at the atomic level

and can result in the formation of unwanted byproducts [31,32]. Furthermore, HER is a kinetically favorable two-electron process, consuming fewer electrons and requiring a lower electrical potential (E^0 = 0 V_{RHE}) than the NO_3RR. Therefore, catalyst designs that optimize HER suppression should be considered. Finally, practical systems produce considerable gaseous byproducts such as hydrogen in the potential range of the NO_3RR. The gaseous products make bubbles that block the surfaces of the catalyst and electrode, thereby decreasing mass transfer and NO_3RR performance [33,34]. Controlling surface hydrophobicity is important for achieving high current density NO_3RR systems; however, this issue remains underestimated.

Hereafter, the design strategies of Cu-SACs that can easily tune their electronic structure and surface properties are introduced, and the NO_3RR performances of these catalysts are discussed.

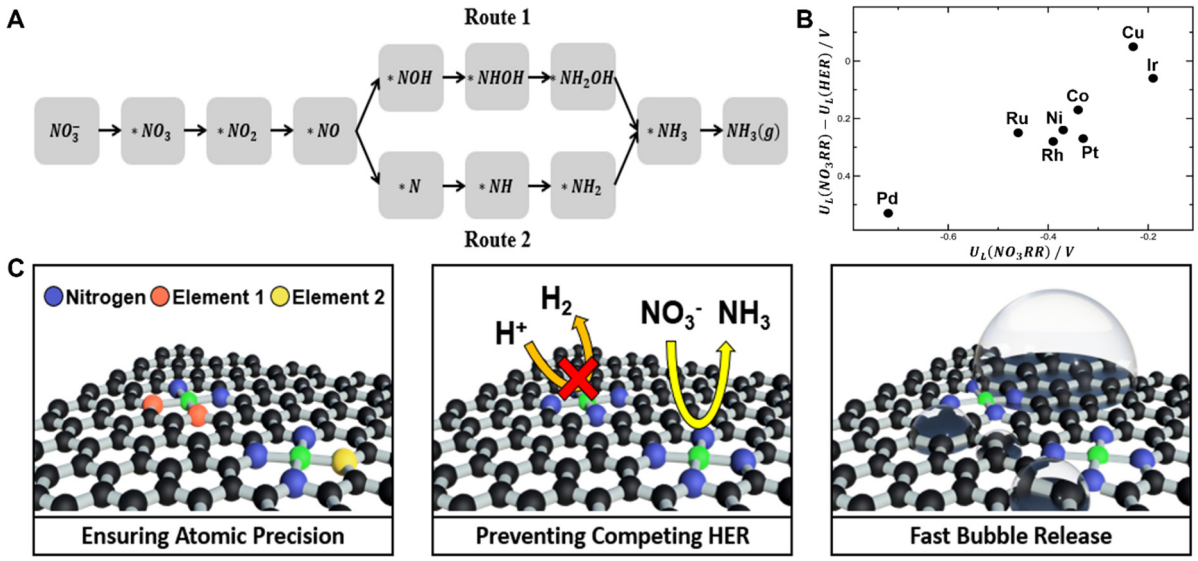

Figure 1. Understanding nitrate reduction mechanism and challenges of single-atom catalysts in electrochemical ammonia production. (**A**) Proposed NH_3 formation routes via *NO intermediates: stepwise hydrogenation (Route 1) and deoxygenation–hydrogenation (Route 2). Reproduced with permission. (**B**) Selectivity map of NO_3RR versus HER on various metals, highlighting Cu as a favorable catalyst. Reproduced with permission [24]. Copyright 2023, Royal Society of Chemistry. (**C**) Key challenges in NO_3RR using single-atom catalysts including HER competition, atomic arrangement control, and fast bubble release.

3. Cu-Based Single-Atom Catalyst Designs for Efficient Electrochemical NO_3RR

3.1. Cu Single-Atom Catalysts in N Containing Carbon

The metal–N_4 structure, in which the central metal atom is coordinated with four pyridinic N, is common in single-atom materials and the central Cu accepts electrons from the surroundings. Liu et al. reported a pyridinic-N-rich Cu single-atom catalyst (PR-CuNC) synthesized via a two-step process involving the formation of polypyrrole-polyethyleneimine hydrogels and the pyrolysis of Cu-impregnated hydrogels [35]. High-angle annular dark-field scanning transmission electron microscopy (HAADF-STEM) and energy-dispersive X-ray spectroscopy (EDS) confirmed the even distribution of single Cu atoms within a carbon-N matrix (Figure 2A). X-ray photoelectron spectroscopy (XPS) detected Cu in both the Cu(I) and Cu(II) states, with a higher Cu(I) proportion than the Cu(II) proportion in PR-CuNC owing to the coordination of pyridinic N (Figure 2B). X-ray absorption near-edge structure (XANES) and extended X-ray adsorption fine structure (EXAFS) analyses confirmed the Cu-N_4 configuration, predominantly with pyridinic N, which influences the electron configuration of Cu (Figure 2C,D).

PR-CuNC exhibited higher current densities than low pyridinic-N coordinated Cu (CuNC) during NH_3 production, achieving a FE of 94.61% and an NH_3 yield rate of 130.71 $mg/mg_{Cu}^{-1}\cdot h^{-1}$ (Figure 2E). The PR-CuNC maintained high NH_3 selectivity across various potentials, producing minimal byproducts such as NO_2^- or N_2 gas (Figure 2F). Stability tests revealed consistent performance over multiple cycles, with no notable decline in activity or selectivity. Density function theory (DFT) calculations demonstrated the superior activity of the PR-CuNC stems to the pyridinic-N-rich coordination around the single Cu atoms, lowering the energy barrier for the rate-determining step of NO_3^- reduction. Cu-pyridinic-N_4 sites facilitate stronger NO_3^- adsorption and electron transfer owing to favorable electronic hybridization between Cu and N orbitals, unlike the Cu-pyrrolic-N_4 sites (Figure 2G,H). This configuration suppresses the HER by increasing the energy barrier for water dissociation, enhancing

ammonia selectivity. As atomic-scale structure analysis of CuNC using XANES and EXAFS has not been documented, the direct relationship between the local coordination structures at Cu (pyridinic-N_4 or pyrrolic-N_4) and the electrochemical NO_3RR performances is unclear; however, electron transfer at the single Cu sites considerably influences the NO_3RR activity.

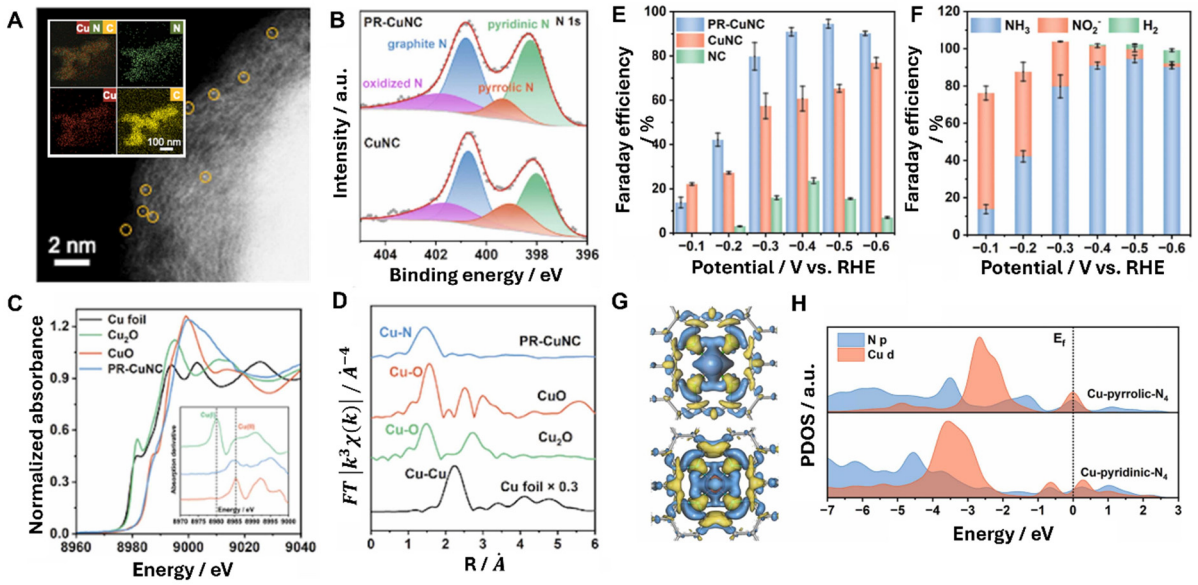

Figure 2. Structure–activity relationship of pyridinic-N-rich Cu single-atom catalyst (PR-CuNC) for NO_3RR. (**A**) HAADF-STEM and EDS mapping showing atomically dispersed Cu atoms. (**B**) N 1s XPS spectra indicating increased pyridinic-N content in PR-CuNC. (**C**) FE of NH_3 production over PR-CuNC, CuNC, and NC at various potentials. (**D**) Product distribution showing suppressed NO_2^- and H_2 formation. (**E**) Cu K-edge XANES spectra revealing Cu oxidation states. (**F**) EXAFS spectra supporting the identification of Cu–N_4 coordination. (**G**) Charge density difference plots of Cu–N_4 sites. (H) PDOS analysis showing enhanced Cu–N hybridization at pyridinic-N_4 sites. Reproduced with permission [35]. Copyright 2024, Elsevier.

Moreover, Zhu et al. reported the importance of isolated single Cu atoms for enhancing the NO_3RR [36]. Cu–N–C-800 was synthesized via a pyrolysis process using a Cu-based metal-organic framework (Cu-BTC; BTC represents 1,3,5-benzenetricarboxylic acid). The Cu-BTC mixture was pyrolyzed at 800 °C in an Ar atmosphere, yielding carbon nanosheets with isolated Cu atoms coordinated with N. The annealing temperature is critical as it influences the size and dispersion of Cu; single atoms are formed at 800 °C, and temperatures higher than 800 °C (e.g., 900 °C or 1000 °C) cause nanoparticle aggregation. STEM images revealed that Cu-N-C-800 exhibited a 2D nanosheet morphology with wrinkles embedding single Cu atoms within a carbon-N matrix (Figure 3A). XPS analysis revealed that Cu was present in mixed Cu(0)/Cu(I) and Cu(II) states, with a higher pyridinic-N content in Cu–N–C-800, enhancing Cu-N coordination (Figure 3B). XANES and EXAFS data indicate the presence of a Cu-N_x structure (predominantly Cu-N_2 and Cu-N_4), with Cu valence between Cu(0) and Cu(II), leaning toward Cu(I) (Figure 3C).

Cu–N–C-800 demonstrates exceptional performance when used in the NO_3RR, achieving a 97.3% nitrate conversion yield over 12 h at −1.3 V_{RHE} and exhibiting a mass activity of 4.2 × 10^{-3}·s^{-1}·g^{-1}_{Cu}, significantly outperforming Cu–N–C-700, Cu–N–C-900, Cu–N–C-1000, and Cu plate-800 (Figure 3D). Cu–N–C remains stable over 20 cycles, with minimal activity loss (5.4% drop), and performs effectively across varying potentials and nitrate concentrations and in the presence of chloride, highlighting the robustness and selectivity of Cu–N–C for nitrate-to-ammonia conversion (Figure 3E). The enhanced activity of Cu–N–C-800 originated from single-atom Cu sites coordinated with N, imparting higher adsorption energies to NO_3^- (−4.06 eV) and NO_2^- compared to that of the Cu(111) surfaces (6.13 eV corresponding to NO_3^-). DFT calculations reveal that these Cu–N_x sites lower the energy barrier for NO_3^- reduction and facilitate NO_2^- conversion, slowing the release of the ion into the solution.

Recently, Yang et al. reported the structural evolution of a Cu–N–C single-atom catalyst used in an electrochemical reaction, improving NO_3RR performances and the redispersion of Cu into single atom sites [37]. Single atom catalysts with a Cu–N_4 structure were synthesized, and the Cu–N–C atomic configuration was characterized. HAADF-STEM and EXAFS analyses revealed no Cu–Cu bonding and a Cu–N bond length of 1.92

Å (Figure 3F). The coordination number (CN) of Cu–N was calculated to be 3.7, with no detectable Cu–Cu scattering in the EXAFS spectra.

The linear sweep voltammetry curve of Cu–N–C in 0.1 M KOH and 0.1 M KNO_3 reveals a substantial increase in current density and an onset potential shift to 0.136 V_{RHE} in the presence of NO_3^-; the potential shift in the absence of NO_3^- was −0.5 V_{RHE}, outperforming the N–C support threefold during NH_3 production. At −1.0 V_{RHE}, a maximum NH_3 production rate of 4.5 mg cm^{-2} h^{-1} (12.5 mol_{nh3} g_{Cu}^{-1} h^{-1}) was achieved with a FE of 84.7%, verified via nuclear magnetic resonance spectroscopy using ^{15}N-labeled NO_3^-. Under electrocatalytic conditions, operando X-ray absorption spectroscopy reveals dynamic restructuring. At 0.0 V_{RHE}, the CN reduces to 2.8, forming Cu–N_3, and at negative potentials (e.g., −1.00 V_{RHE}), Cu(0) was immediately formed and aggregated into nanoparticles (~5–10 nm) (Figure 3G). Interestingly, exposure to air after electrolysis re-oxidizes Cu(0), restoring Cu–N_4 structure. This observation suggests that the Cu nanoparticles form during NO_3RR, rather than the as-synthesized Cu–N_4 structure are the real active sites (Figure 3H). However, the true active foams of Cu-SACs for NO_3RR have not been fully elucidated, and this topic will be discussed in the outlook section.

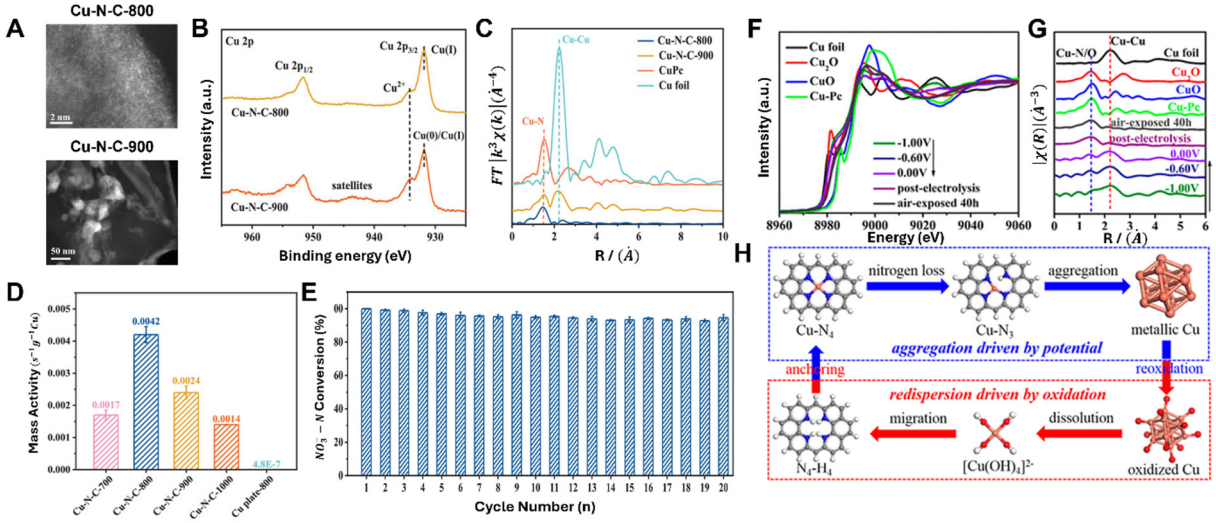

Figure 3. Cu–N–C single-atom catalysts and their structural evolution during NO_3RR. (**A**) TEM images of Cu–N–C-800 and Cu–N–C-900. (**B**) Cu 2p XPS spectra showing oxidation states. (**C**) EXAFS spectra indicating Cu–N and Cu–Cu coordination. (**D**) Mass activity comparison among Cu–N–C catalysts and Cu foil. (**E**) NO_3^--to-NH_3 conversion efficiency over 20 cycles showing catalyst stability. Reproduced with permission [36]. Copyright 2020, Wiley-VCH. Potential-driven restructuring of Cu single atoms and (**F**) XANES and (**G**) EXAFS showing Cu aggregation under negative potentials. (**H**) Schematic illustrating reversible redispersion and coordination recovery upon oxidation. Reproduced with permission [37]. Copyright 2022, American Chemical Society.

3.2. Cu Single-Atom Catalysts in Desymmetrized Anion Containing Carbon

Coordination desymmetrization at a central Cu site is a promising strategy for designing single-atom catalysts. Gu et al. reported a Cu–N_1O_2 catalyst prepared using melamine and cyanuric acid using a pyrolysis-assisted method [38]. The desymmetrization of the coordination environment was achieved using deionized water rather than dimethyl sulfoxide, generating a synthetic scaffold for the synthesis of Cu–N_1O_2. Atomic-level characterization revealed the presence of well-dispersed Cu atoms anchored to N/O coordination sites via Cu–N_1O_2 coordination (Figure 4A). To distinguish between the similar binding energies of Cu^0 and Cu^+, the valence states were investigated via LMM Auger spectroscopy. As the 1^G and 1^F peaks corresponded to the Cu(0) and, Cu(I) and Cu(II) species, respectively, Cu–N_1O_2 and Cu–N_2O_2 were concluded to contain certain quantities of Cu(0), whereas Cu(II) was dominant in Cu–N_3 and Cu–N_4 (Figure 4B). These results demonstrate that N/O coordination donates more electrons to the Cu in Cu–N_xO_x than to the Cu in Cu–N_x.

Electrochemical tests demonstrate that Cu–N_1O_2 outperformed conventional Cu–N_4 during the electrochemical NO_3RR, exhibiting a FE of 96.5% at −0.6 V_{RHE} and 82.1% at −0.89 V_{RHE}, respectively (Figure 4C). Furthermore, Cu–N_1O_2 yielded a high NH_3 formation rate of 3120 μg h^{-1} cm^{-2} and current density of 39.7 mA cm^{-2}. Stability tests demonstrated prolonged catalytic performance with minimal structural degradation after continuous operation. The superior catalytic activity of Cu–N_1O_2 can be attributed to the unique coordination environment and optimized electronic structure. In situ electrochemical Raman spectra analysis revealed that the characteristic peaks of NH_3 at 1141 cm^{-1} and those of the NO in NO_2^- at 1201 cm^{-2} appeared in the spectrum of

Cu–N_1O_2 at −0.2 V_{RHE}. However, these peaks were obtained at −0.8 V_{RHE} in the spectrum of Cu–N_4 (Figure 4D,E). This result indicates that Cu–N_1O_2 converts NO_3^- to NH_3, effectively requiring a small amount of electrical energy. DFT calculation results confirmed that introducing O facilitates the NO_3RR. Cu–N_1O_2 exhibits a lower energy barrier to $*NO_2 \rightarrow *NO$, with a value of 0.64 eV, than Cu-N_4. Moreover, unsaturated coordination environments, such as those in Cu–N_1O_2 and Cu–N_3, exhibit lower energy barriers than those of coordinatively saturated environments such as Cu–N_2O_2 and Cu–N_4, referring to the substantial contribution of the unsaturated coordination condition at the central atom to the NO_3RR. Similarly, Cheng et al. investigated the effects owing to the atomic configuration of the N/O in the *cis* position in Cu–N_2O_2 on the electrochemical NO_3RR [39]. Cu–*cis*–N_2–O_2 was synthesized via pyrolysis using a salen ligand as the *cis*–N/O agent; Cu–*cis*–N_2–O_2 exhibited enhanced NO_3RR performances.

The formation of unbalanced coordinative symmetry at central Cu sites is an effective catalyst design strategy; however, owing to the difficult structural analysis techniques and the precise control of the atomic configuration, limited examples have been reported.

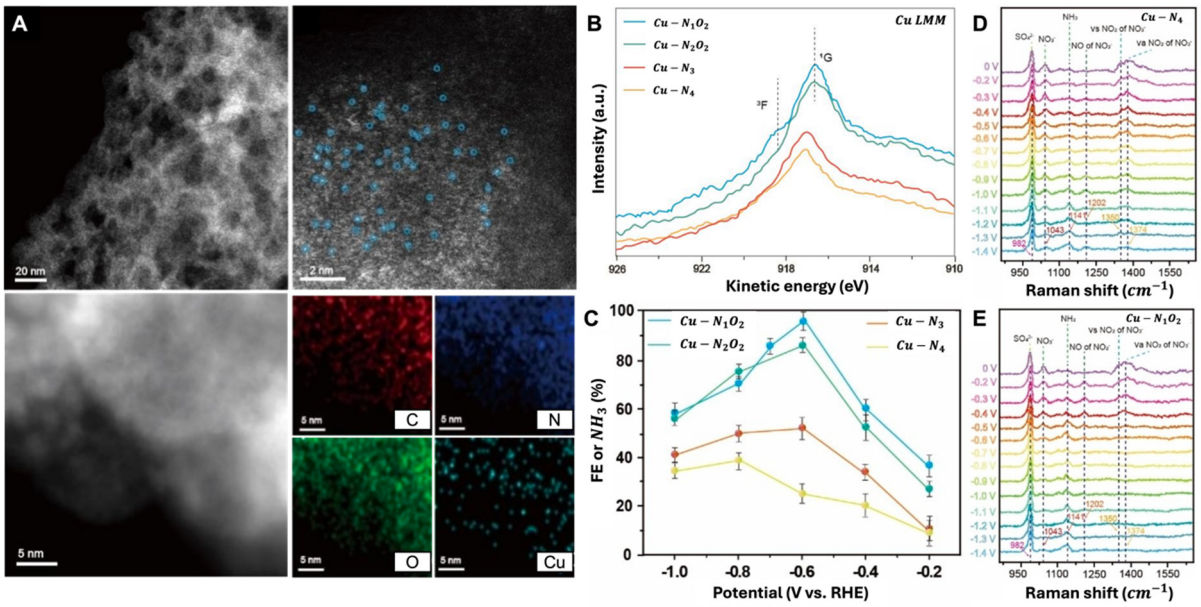

Figure 4. Coordination desymmetrization enhances NO_3RR activity of Cu–N_1O_2 catalysts. (**A**) HAADF-STEM and EDS mapping showing atomically dispersed Cu atoms coordinated by N and O atoms. (**B**) LMM Auger spectra indicating higher Cu^0 content in Cu–N_1O_2 and Cu–N_2O_2 compared to Cu–N_3 and Cu–N_4. (**C**) FE of NH_3 production at various applied potentials, with Cu–N_1O_2 achieving a peak FE of 96.5%. (**D**,**E**) In situ Raman spectra of (**D**) Cu–N_4 and (**E**) Cu–N_1O_2, showing earlier appearance of $*NO_2$ (1201 cm^{-1}) and NH_3 (1141 cm^{-1}) peaks for Cu–N_1O_2, indicating improved NO_3RR kinetics at lower overpotentials. Reproduced with permission [38]. Copyright 2024, Wiley-VCH.

3.3. Cu Based Multi-Element Single-Atom Catalysts in N Containing Carbon

A Fe/Cu diatomic catalyst was developed by anchoring active metal atoms (Fe and Cu) into holey N-doped graphene (HNG) [40]. HNG was synthesized by sonicating graphene oxide in nitric acid, creating edge sites suitable for metal binding. Thereafter, Fe and Cu precursors were added, forming Fe/Cu dual atoms loaded onto the N-edge of micropores (Fe/Cu-HNG) (Figure 5A). The Fe/Cu-HNG exhibited a "Y-type" ML_3 coordination structure, in which two N atoms and one metal atom formed a dimer structure inside the holes. Elemental mapping revealed the uniform distribution of C, N, Fe, and Cu on the graphene surface, and the structural characterization of Fe/Cu-HNG revealed that Fe and Cu atoms formed diatomic pairs with an average bond length of 2.3 ± 0.2 Å. XPS analysis indicated electron transfer from Fe to Cu, evidenced by the shifts in binding energies of the Fe 2p and Cu 2p peaks.

Fe/Cu-HNG demonstrated outstanding electrochemical NO_3RR performance, a maximum FE of 92.51% at −0.3 $V_{RHE,}$ and a high NH_3 yield rate of 1.08 mmol h^{-1} mg^{-1} at −0.5 V_{RHE} (Figure 5B). DFT calculations attribute the excellent activity of Fe/Cu-HNG to the strong NO_3^- adsorption at the Y-type ML_3 dual-atom sites, as illustrated in Figure 5C. The binding energy of NO_3 in Fe/Cu-HNG was −1.19 eV, higher than those of Fe-HNG (−0.89 eV) and Cu-HNG (−0.56 eV). This strong NO_3 bond lowers the energy barrier of the first electron discharge ($* + NO_3^-$

→ *NO_3 + e^-) and, after the adsorption of NO_3, negative polarization promotes deoxygenation and hydrogenation (Figure 5D).

Moreover, Wang et al. reported a Cu–Ni dual-single-atom catalyst (Cu/Ni–NC) synthesized using a Cu- and Ni-embedded zeolitic imidazolate framework as a precursor, followed by pyrolysis at 950 °C [41]. HAADF-STEM and EDS verified the uniform dispersion of Cu and Ni atoms (Figure 5E). Cu/Ni–NC exhibited superior NO_3RR performance, achieving an FE of 97.28% at −0.7 V_{RHE} and outperforming single-atom catalysts (Cu–NC: 33.2% and Ni–NC: 15.2%). Byproduct formation (NO_2^-) was effectively suppressed, and stability was maintained over an hour (Figure 5F,G). The enhanced NO_3RR performance of Cu/Ni–NC with respect to those of Cu–NC and Ni–NC can be attributed to the electron localization around Cu–O–*NO_3^-–O-Ni. Strong hybridization between the Cu 3d–Ni 3d orbitals with the O 2p orbitals of NO_3^- enhanced adsorption and reaction kinetics (Figure 5H). The total number of electrons transferred from Cu (0.32 e) and Ni (0.27 e) to *NO_3^- were higher than those in the case of Cu–NC and Ni–NC, which was 0.3 e^- and 0.24 e^-, respectively, indicating strong interactions between the catalyst and NO_3^-.

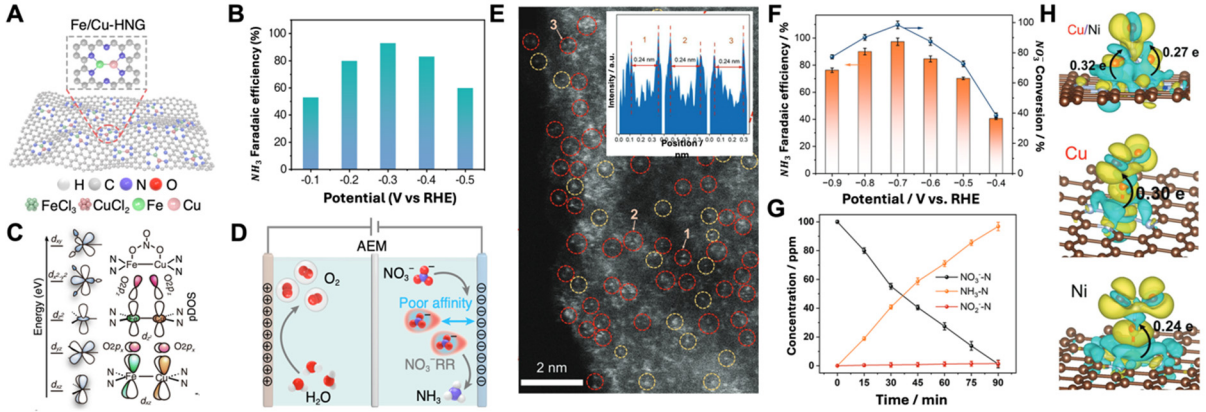

Figure 5. Fe/Cu-HNG catalyst with Y-type ML_3 coordination for NO_3^- activation. (**A**) Schematic of Fe/Cu dual atoms anchored on holey N-doped graphene. (**B**) Faradaic efficiency of NH_3 production with a peak FE of 92.5% at −0.3 V. (**C**) Orbital interaction-driven NO_3^- adsorption at Fe/Cu dual sites. (**D**) negative electrode surface polarization for enhanced NO_3RR. Reproduced with permission [40]. Copyright 2023, Springer Nature. Cu/Ni dual-single-atom catalyst with enhanced selectivity via 3d–3d hybridization. (**E**) HAADF-STEM image showing atomically dispersed Cu and Ni atoms. (**F**) NH_3 production and FE across potentials. (**G**) Time-dependent NO_3^- conversion and NH_3 yield. (**H**) Charge density plots showing strong electron transfer at Cu/Ni dual sites. Reproduced with permission [41]. Copyright 2023, Wiley-VCH.

3.4. Cu Single-Atom Embedded Metal Oxide Catalysts

Since NO_3RR requires a balanced electrochemical reaction involving simultaneous proton generation and NO_3^- hydrogenation, Cu single-atom embedded metal oxides may exhibit enhanced NO_3RR performance compared to pure Cu-SACs. Shen et al. addressed the limitations of scaling relations by developing a dual-driven single-atom Cu catalyst supported on tungsten oxide (Cu_1/WO_3) [42]. The catalyst featured WO_3 as the water dissociation component that provided protons to the Cu_1 site, while the electron-deficient Cu_1 site facilitated the selective conversion of NO_3^- to NH_3. In the synthesis process, oxygen vacancies within WO_3 nanosheets serves as anchoring sites for Cu atoms, yielding substantial Cu content (4.07 wt%). HRTEM results confirmed the Cu single-atom embedded WO_3 nanosheet structures (Figure 6A). EXAFS validated the Cu–O–W bonding arrangement and ruled out the presence of Cu clustering (Figure 6B,C).

Performance evaluation comparing Cu_1/WO_3 and Cu nanoparticle catalysts (Cu NPs/C) revealed that Cu_1/WO_3 showed a mass activity of 1274.4 $mg_N\ h^{-1}\ g_{Cu}^{-1}$, NH_3 selectivity of 99.2%, and a FE of 93.7% at −0.60 V_{RHE}. Specifically, NH_3 concentration was increased along reaction time in Cu_1/WO_3, whereas Cu NPs/C accumulated NO_2^- intermediates (Figure 6D). DFT calculations further demonstrate that electron-deficient Cu_1 centers exhibit strong affinity for N-containing intermediates, facilitating their reduction while minimizing unwanted NO_2^- byproduct formation (Figure 6E).

Also, Liu et al. reported cooperative effects between Cu single-atom and cobalt oxide through their complementary ion affinities [43]. Cu single-atom catalysts supported on cobalt oxide (Co_3O_4/Cu_1-N-C) have shown improved NO_3RR activity through a tandem structure. Two-step process was introduced to form Co_3O_4/Cu_1-N-C: initial preparation of Cu_1-N-C through pyrolysis of Cu-doped zeolitic imidazolate framework

(ZIF-8), followed by deposition of Co_3O_4 nanosheets onto the Cu_1-N-C (0.60 wt% Cu and 4.70 wt% Co) (Figure 6F). Co_3O_4/Cu_1-N-C exhibited an ammonia yield rate of 114.0 mg_{NH3} h^{-1} cm^{-2} and a FE of 97.7% at −0.8 V_{RHE}, outperforming those of Co_3O_4/N-C and Cu_1-N-C (Figure 6G).

Kinetic studies calculating rate constants for NO_3^- electroreduction (k_1) and NO_2^- electroreduction (k_2) revealed complementary roles of the catalyst components. The results showed that Cu_1-N-C demonstrated high activity for the initial NO_3^- to NO_2^- conversion (high k_1 and low k_2), while Co_3O_4 specialized in the subsequent NO_2^- to NH_3 transformation (low k_1 and high k_2). The Co_3O_4/Cu_1-N-C achieved optimal performances in both reaction steps, exhibiting high k_1 and k_2 values, facilitating complete NO_3^- to NH_3 conversion (Figure 6H). Adsorption capacity (q_e) measurements for NO_3^- and NO_2^- species demonstrated that Co_3O_4/Cu_1-N-C possessed the highest binding affinity for both NO_3^- and NO_2^- compared to Co_3O_4/N-C and Cu_1-N-C (Figure 6I). The q_e results confirmed that the integration of Cu_1-N-C with Co_3O_4 enhanced the processing of both NO_3^- and NO_2^- species.

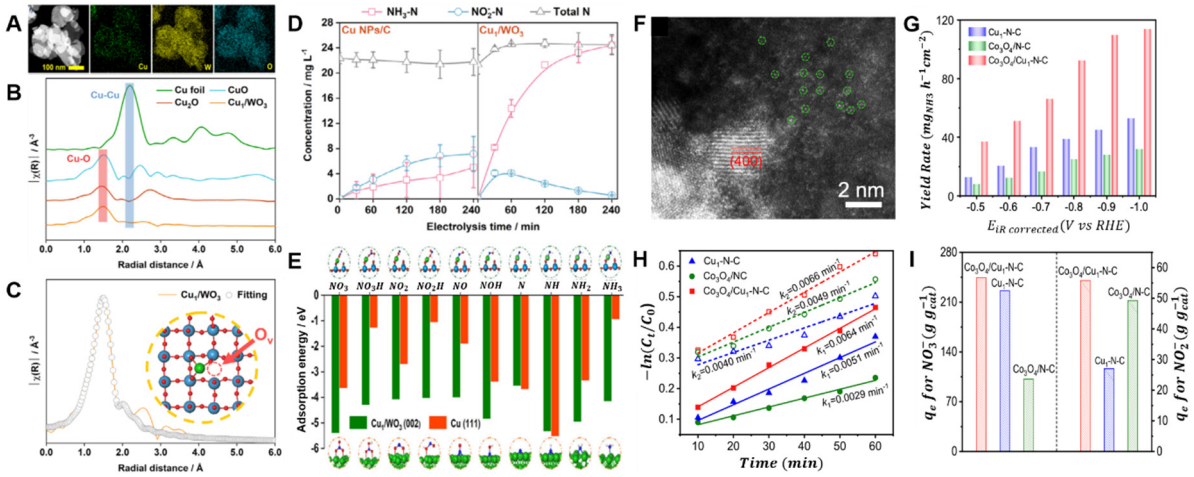

Figure 6. (**A**) Elemental mapping of Cu, W, and O on Cu_1/WO_3. (**B**) FT-EXAFS showing isolated Cu–O coordination without Cu aggregation and (**C**) EXAFS fitting results. (**D**) Comparison of product distribution of Cu_1/WO_3 and Cu NPs/C at −0.60 V. (**E**) DFT-calculated adsorption energies on Cu_1/WO_3(002) and Cu(111). Reproduced with permission [42]. Copyright 2025, Wiley-VCH. (**F**) Aberration-corrected HAADF-STEM image of Co_3O_4/Cu_1-N-C. (**G**) NH_3 yield rate comparison and (**H**) kinetic plots and (**I**) adsorption capacity (q_e) results of Co_3O_4/Cu_1-N-C, Co_3O_4/NC, and Cu_1-N-C. Reproduced with permission [43]. Copyright 2024, Springer Nature.

4. Conclusions and Outlook

This minireview examines Cu-SACs which are considered promising catalysts for the electrochemical NO_3RR. Atomic-scale tuning strategies such as modifying the coordination number, desymmetrizing the active site, introducing secondary metallic species, and creating heterointerfaces by embedding SACs in metal oxides have been adopted to optimize the stereospecific geometrical properties of Cu-SACs. Among them, desymmetrization of surrounding elements at Cu center has emerged as a scalable, organometallic-inspired approach for tailoring the electronic structures of the active sites, thereby guiding the next-generation SACs design. However, progress remains limited because single-atom sites are difficult to characterize and limited synthetic methods afford atomic precision in both composition and spatial placement.

Recently developed catalysts and their key metrics are listed in Table 1. The electrochemical NO_3RR exhibits relatively high FE values over 90%, unlike other multi-electron participating reactions such as the N_2, CO, or CO_2 reduction reactions [1,44,45]. Nonetheless, significant efforts are required to advance the Cu-SACs for practical NO_3RR system.

Scale-up To increase NH_3 yields for large-scale production, the NO_3RR evaluation should adopt membrane electrode assembly (MEA)-based electrochemical technology which exhibits high NH_3 production rates. Systematic optimization of MEA cells, electrodes, catalysts, and membranes is needed to improve mass transfer, specific activity, ion transfer, and so on.

Advanced Characterization and Measurement Protocols Standard measurement protocols of the electrochemically active surface area (ECSA) of SACs are required. The ECSA of SACs is generally evaluated by double layer capacitances. However, those ECSAs are different from chemically active surface areas and the extent to which a single-atom site is engaged in the electrochemical reaction cannot be calculated. Thus, developing

standard methods for evaluating ECSA like 'under potential deposition' for SACs is required to quantify active-site densities and properties.

Enhancing Catalyst Stability and Durability Migration and coalescence of isolated Cu atoms on carbon supports reduce active-site density and, in turn, NO_3RR performance. Although Yang et al. identified in-situ formed metallic Cu as the active sites [37], other reports activity losses attributable to aggregation [36]. Robust Cu-SACs will therefore depend on local coordination engineering and the incorporation of secondary metals to create di- or tri-atomic motifs that resist sintering while retaining high activity.

Finally, we intend that this mini-review facilitates the development of Cu-based single atoms for the electrochemical NO_3RR and provides valuable insights to the researchers in the fields of nanochemistry and materials science.

Table 1. Summary of representative electrocatalysts for nitrate reduction to ammonia.

Catalysts	Applied Potential (V vs. RHE)	Current Density ($mA\ cm^{-2}$)	Fe (%)	Ammonia Yield		Stability Test Time (h)	Electrolyte		Ref.
				$mmol\ h^{-1}\ mg_{cat}^{-1}$/($mmol\ h^{-1}\ cm^{-2}$)	Reaction Time (h)		NO_3^-(M)	Background	
PR-CuNC	−0.5	−52.2	94.6	7.67	0.5	5	0.1	0.1M KOH	[35]
Cu-N-C SAC	−1.00	−47.2	84.7	12.5	0.5	10	0.1	0.1M KOH	[37]
Cu-N_1O_2	−0.6	−37.4	96.5	(0.18)	6	800	0.01	0.1M KOH	[38]
$\mathbf{Cu-cis-N_2O_2}$	−1.2	−144.5	88.5	(1.687)	1	2000	0.071	0.5 M Na_2SO_4	[39]
Fe/Cu-HNG	−0.3	−36.4	92.5	0.64	3	24	0.1	1.0 M KOH	[40]
Cu/Ni–NC	−0.7	−64.9	97.3	(0.324)	1.5	30	0.001	0.5 M Na_2SO_4	[41]
$\mathbf{Cu_1/WO_3}$	−0.6	−1.35	93.7	2.23	4	48	0.006	0.05 M Na_2SO_4	[42]
$\mathbf{Co_3O_4/Cu_1-N-C}$	−1	−1732	97.7	(6.69)	0.167	3.33	1	1M KOH	[43]
Cu MNC − 7	−0.64	−9.94	93.9	8.606	6	85	0.007	0.05 M Na_2SO_4	[46]
Cu − NC	−0.89	−44.5	82.1	0.1611	0.5	12	0.2	0.2 M Na_2SO_4	[47]
$\mathbf{Cu-N_4B_2}$	−0.6	−179.8	98.2	(4.5)	5	30	0.1	1M KOH	[48]
o-CoP/C@Cu3P/CF	−0.25	−312.4	96.2	(1.57)	1	10	0.1	1.0 M KOH	[49]
Au/Cu SAAs	−0.8	−95.9	99.7	(0.193)	1.5	30	0.007	0.5 M Na_2SO_4	[50]
PdCu SAA	−0.6	−49.7	97.1	(0.015)	1	10	0.007	0.5 M Na_2SO_4	[51]
Ni_1Cu-SAA	−0.55	−117.1	~100	(0.327)	1.1	8.9	0.02	0.5 M K2SO4	[52]
AumCu SAAAs	−0.8	−434.5	99.9	(6.21)	1	400	0.1	1 M KOH	[53]
Co─Cu SCC	−0.4	−14.6	92.1	0.1	0.5	24	0.1	0.1 M KOH	[54]
$\mathbf{Cu_1/CeO_2}$	−0.8	−	91.3	6.37	2	120	0.06	1.7M NaCl	[55]
$\mathbf{TiO_2-Cu}$	−0.4	−0.231	62.2	0.034	6	36	0.002	0.5 M Na_2SO_4	[56]
$\mathbf{CuCoO_X}$	−1.3	−16.88	93.3	(0.026)	2	20	0.004	0.5 M Na_2SO_4	[57]
$\mathbf{Cu-Fe_3O_4-5}$	−0.6	−57.72	~100	(0.421)	0.33	-	0.1	0.1 M KOH	[58]
$\mathbf{I_1Cu_4}$	−0.65	−89.6	98.5	(0.256)	4	100	0.007	0.5 M K_2SO_4	[59]
$\mathbf{CuF_{16}Pc/C}$	−0.9	−	96.8	(0.459)	4	20	0.002	0.05 M Na_2SO_4	[60]
Cu − F	−1.2	−1377	96.2	(5.22)	1	24	0.2	1.0 M KOH + 0.5M KF	[61]

Author Contributions

H.B.P.: conceptualization, writing—original draft preparation, visualization; H.J.: supervision, writing—reviewing and editing. funding acquisition. All authors have read and agreed to the published version of the manuscript.

Funding

This work was financially supported by the National Research Foundation of Korea (2022R1C1C2005786) and the Korea Institute of Science and Technology (Grant no. 2E33901). Also, this research was supported by the BK21 FOUR (Fostering Outstanding Universities for Research, No. 2120241915488) funded by the Ministry of Education (MOE, Korea) and National Research Foundation of Korea (NRF).

Conflicts of Interest

The authors declare no conflict of interest.

Use of AI and AI-assisted Technologies

No AI tools were utilized for this paper.

References

1. Jin, H.; Kim, S.S.; Venkateshalu, S.; et al. Electrochemical Nitrogen Fixation for Green Ammonia: Recent Progress and Challenges. *Adv. Sci.* **2023**, *10*, 2300951. https://doi.org/10.1002/advs.202300951.

2. Valera-Medina, A.; Amer-Hatem, F.; Azad, A.K.; et al. Review on Ammonia as a Potential Fuel: From Synthesis to Economics. *Energy Fuels* **2021**, *35*, 6964–7029. https://doi.org/10.1021/acs.energyfuels.0c03685.
3. Hasan, M.H.; Mahlia TM, I.; Mofijur, M.; et al. A comprehensive review on the recent development of ammonia as a renewable energy carrier. *Energies* **2021**, *14*, 3732. https://doi.org/10.3390/en14133732.
4. Chyong, C.K.; Italiani, E.; Kazantzis, N. Energy and climate policy implications on the deployment of low-carbon ammonia technologies. *Nat. Commun.* **2025**, *16*, 776. https://doi.org/10.1038/s41467-025-56006-6.
5. El-Shafie, M.; Kambara, S. Recent advances in ammonia synthesis technologies: Toward future zero carbon emissions. *Int. J. Hydrogen Energy* **2023**, *48*, 11237–11273. https://doi.org/10.1016/j.ijhydene.2022.09.061.
6. Salmon, N.; Bañares-Alcántara, R. Green ammonia as a spatial energy vector: A review. *Sustain. Energy Fuels* **2021**, *5*, 2814–2839. https://doi.org/10.1039/D1SE00345C.
7. Wang, B.; Li, T.; Gong, F.; et al. Ammonia as a green energy carrier: Electrochemical synthesis and direct ammonia fuel cell—A comprehensive review. *Fuel Process. Technol.* **2022**, *235*, 107380. https://doi.org/10.1016/j.fuproc.2022.107380.
8. Kojima, Y.; Yamaguchi, M. Ammonia as a hydrogen energy carrier. *Int. J. Hydrog. Energy* **2022**, *47*, 22832–22839. https://doi.org/10.1016/j.ijhydene.2022.05.096.
9. Humphreys, J.; Lan, R.; Tao, S. Development and Recent Progress on Ammonia Synthesis Catalysts for Haber–Bosch Process. *Adv. Energy Sustain. Res.* **2021**, *2*, 2000043. https://doi.org/10.1002/aesr.202000043.
10. Erfani, N.; Baharudin, L.; Watson, M. Recent advances and intensifications in Haber-Bosch ammonia synthesis process. *Chem. Eng. Process. Process Intensif.* **2024**, *204*, 109962. https://doi.org/10.1016/j.cep.2024.109962.
11. Appl, M. The Haber-Bosch heritage: The ammonia production technology. In Proceedings of the 50th Anniversary of the IFA Technical Conference, Sevilla, Spain, 25–26 September 1997.
12. Kim, H.S.; Jin, H.; Kim, S.H.; et al. Sacrificial Dopant to Enhance the Activity and Durability of Electrochemical N2 Reduction Catalysis. *ACS Catal.* **2022**, *12*, 5684–5697. https://doi.org/10.1021/acscatal.2c00089.
13. Jin, H.; Kim, H.S.; Lee, C.H.; et al. Directing the Surface Atomic Geometry on Copper Sulfide for Enhanced Electrochemical Nitrogen Reduction. *ACS Catal.* **2022**, *12*, 13638–13648. https://doi.org/10.1021/acscatal.2c03680.
14. Mingolla, S.; Rosa, L. Low-carbon ammonia production is essential for resilient and sustainable agriculture. *Nat. Food* **2025**, *6*, 610–621. https://doi.org/10.1038/s43016-025-01125-y.
15. Hollevoet, L.; De Ras, M.; Roeffaers, M.; et al. A. Energy-Efficient Ammonia Production from Air and Water Using Electrocatalysts with Limited Faradaic Efficiency. *ACS Energy Lett.* **2020**, *5*, 1124–1127. https://doi.org/10.1021/acsenergylett.0c00455.
16. Tang, C.; Qiao, S.-Z. How to explore ambient electrocatalytic nitrogen reduction reliably and insightfully. *Chem. Soc. Rev.* **2019**, *48*, 3166–3180. https://doi.org/10.1039/C9CS00280D.
17. Zhang, X.; Wang, Y.; Liu, C.; et al. Recent advances in non-noble metal electrocatalysts for nitrate reduction. *Chem. Eng. J.* **2021**, *403*, 126269. https://doi.org/10.1016/j.cej.2020.126269.
18. Jia, S.; Sun, X.; Han, B. Electrocatalytic systems for NOx upgrading. *Chem. Commun.* **2025**, *61*, 1262–1274. https://doi.org/10.1039/D4CC05762G.
19. Wang, D.; Lu, X.F.; Luan, D.; et al. Selective Electrocatalytic Conversion of Nitric Oxide to High Value-Added Chemicals. *Adv. Mater.* **2024**, *36*, 2312645. https://doi.org/10.1002/adma.202312645.
20. Chen, G.F.; Yuan, Y.; Jiang, H.; et al. Electrochemical reduction of nitrate to ammonia via direct eight-electron transfer using a copper–molecular solid catalyst. *Nat. Energy* **2020**, *5*, 605–613. https://doi.org/10.1038/s41560-020-0654-1.
21. Deng, X.; Yang, Y.; Wang, L.; et al. Metallic Co Nanoarray Catalyzes Selective NH3 Production from Electrochemical Nitrate Reduction at Current Densities Exceeding 2 A cm^{-2}. *Adv. Sci.* **2021**, *8*, 2004523. https://doi.org/10.1002/advs.202004523.
22. McEnaney, J.M.; Blair, S.J.; Nielander, A.C.; et al. Electrolyte Engineering for Efficient Electrochemical Nitrate Reduction to Ammonia on a Titanium Electrode. *ACS Sustain. Chem. Eng.* **2020**, *8*, 2672–2681. https://doi.org/10.1021/acssuschemeng.9b05983.
23. Bai, L.; Franco, F.; Timoshenko, J.; et al. Electrocatalytic Nitrate and Nitrite Reduction toward Ammonia Using Cu_2O Nanocubes: Active Species and Reaction Mechanisms. *J. Am. Chem. Soc.* **2024**, *146*, 9665–9678. https://doi.org/10.1021/jacs.3c13288.
24. Karamad, M.; Goncalves, T.J.; Jimenez-Villegas, S.; et al. Why copper catalyzes electrochemical reduction of nitrate to ammonia. *Faraday Discuss.* **2023**, *243*, 502–519. https://doi.org/10.1039/D2FD00145D.
25. Choi, J.; Suryanto BH, R.; Wang, D.; et al. Identification and elimination of false positives in electrochemical nitrogen reduction studies. *Nat. Commun.* **2020**, *11*, 5546. https://doi.org/10.1038/s41467-020-19130-z.
26. Liao, G.; Smith, R.L., Jr.; Guo, H.; et al. Review of carbon-based catalysts for electrochemical nitrate reduction and green ammonia synthesis. *Green Chem.* **2024**, *26*, 11797–11831. https://doi.org/10.1039/D4GC04640D.
27. Liao, W.; Wang, J.; Ni, G.; et al. Sustainable conversion of alkaline nitrate to ammonia at activities greater than 2 A cm^{-2}. *Nat. Commun.* **2024**, *15*, 1264. https://doi.org/10.1038/s41467-024-45534-2.
28. Hu, T.; Wang, C.; Wang, M.; et al. Theoretical Insights into Superior Nitrate Reduction to Ammonia Performance of Copper Catalysts. *ACS Catal.* **2021**, *11*, 14417–14427. https://doi.org/10.1021/acscatal.1c03666.

29. Fang, L.; Wang, S.; Song, C.; et al. Boosting nitrate electroreduction to ammonia via in situ generated stacking faults in oxide-derived copper. *Chem. Eng. J.* **2022**, *446*, 137341. https://doi.org/10.1016/j.cej.2022.137341.
30. Chen, H.; Zhang, C.; Sheng, L.; et al. Copper single-atom catalyst as a high-performance electrocatalyst for nitrate-ammonium conversion. *J. Hazard. Mater.* **2022**, *434*, 128892. https://doi.org/10.1016/j.jhazmat.2022.128892.
31. Murphy, E.; Liu, Y.; Matanovic, I.; et al. Elucidating electrochemical nitrate and nitrite reduction over atomically-dispersed transition metal sites. *Nat. Commun.* **2023**, *14*, 4554. https://doi.org/10.1038/s41467-023-40174-4.
32. Long, X.; Zhong, T.; Huang, F.; et al. Exploring microenvironmental configuration effects of Cu-based catalysts on nitrate electrocatalytic reduction selectivity. *Appl. Catal. B Environ. Energy* **2025**, *365*, 124944. https://doi.org/10.1016/j.apcatb.2024.124944.
33. Wang, Y.; Dutta, A.; Iarchuk, A.; et al. Boosting Nitrate to Ammonia Electroconversion through Hydrogen Gas Evolution over Cu-foam@mesh Catalysts. *ACS Catal.* **2023**, *13*, 8169–8182. https://doi.org/10.1021/acscatal.3c00716.
34. Fan, K.; Xie, W.; Li, J.; et al. Active hydrogen boosts electrochemical nitrate reduction to ammonia. *Nat. Commun.* **2022**, *13*, 7958. https://doi.org/10.1038/s41467-022-35664-w.
35. Liu, Y.; Qiu, W.; Wang, P.; et al. Pyridine-N-rich Cu single-atom catalyst boosts nitrate electroreduction to ammonia. *Appl. Catal. B Environ.* **2024**, *340*, 123228. https://doi.org/10.1016/j.apcatb.2023.123228.
36. Zhu, T.; Chen, Q.; Liao, P.; et al. Single-Atom Cu Catalysts for Enhanced Electrocatalytic Nitrate Reduction with Significant Alleviation of Nitrite Production. *Small* **2020**, *16*, 2004526. https://doi.org/10.1002/smll.202004526.
37. Yang, J.; Qi, H.; Li, A.; et al. Potential-Driven Restructuring of Cu Single Atoms to Nanoparticles for Boosting the Electrochemical Reduction of Nitrate to Ammonia. *J. Am. Chem. Soc.* **2022**, *144*, 12062–12071. https://doi.org/10.1021/jacs.2c02262.
38. Gu, Z.; Zhang, Y.; Fu, Y.; et al. Coordination Desymmetrization of Copper Single-Atom Catalyst for Efficient Nitrate Reduction. *Angew. Chem.* **2024**, *136*, e202409125. https://doi.org/10.1002/ange.202409125.
39. Cheng, X.F.; He, J.H.; Ji, H.Q.; et al. Coordination Symmetry Breaking of Single-Atom Catalysts for Robust and Efficient Nitrate Electroreduction to Ammonia. *Adv. Mater.* **2022**, *34*, 2205767. https://doi.org/10.1002/adma.202205767.
40. Zhang, S.; Wu, J.; Zheng, M.; et al. Fe/Cu diatomic catalysts for electrochemical nitrate reduction to ammonia. *Nat. Commun.* **2023**, *14*, 3634. https://doi.org/10.1038/s41467-023-39366-9.
41. Wang, Y.; Yin, H.; Dong, F.; et al. N-coordinated Cu–Ni dual-single-atom catalyst for highly selective electrocatalytic reduction of nitrate to ammonia. *Small* **2023**, *19*, 2207695. https://doi.org/10.1002/smll.202207695.
42. Shen, F.; He, S.; Tang, X.; et al. Breaking Linear Scaling Relation Limitations on a Dual-Driven Single-Atom Copper-Tungsten Oxide Catalyst for Ammonia Synthesis. *Angew. Chem. Int. Ed.* **2025**, *64*, e202423154. https://doi.org/10.1002/anie.202423154.
43. Liu, Y.; Wei, J.; Yang, Z.; et al. Efficient tandem electroreduction of nitrate into ammonia through coupling Cu single atoms with adjacent Co_3O_4. *Nat. Commun.* **2024**, *15*, 3619. https://doi.org/10.1038/s41467-024-48035-4.
44. Zhao, X.; Hu, G.; Chen, G.F.; et al. Comprehensive Understanding of the Thriving Ambient Electrochemical Nitrogen Reduction Reaction. *Adv. Mater.* **2021**, *33*, 2007650. https://doi.org/10.1002/adma.202007650.
45. Kundu, J.; Bhoyar, T.; Park, S.; et al. Recent advances in single- and dual-atom catalysts for efficient nitrogen electroreduction and their perspectives. *Adv. Powder Mater.* **2025**, *4*, 100279. https://doi.org/10.1016/j.apmate.2025.100279.
46. Xue, Y.; Yu, Q.; Ma, Q.; et al. Electrocatalytic Hydrogenation Boosts Reduction of Nitrate to Ammonia over Single-Atom Cu with Cu(I)-N3C1 Sites. *Environ. Sci. Technol.* **2022**, *56*, 14797–14807. https://doi.org/10.1021/acs.est.2c04456.
47. Cheng, J.; Sun, W.; Dai, G.; et al. Electroreduction of nitrate to ammonia on atomically-dispersed Cu-N4 active sites with high efficiency and stability. *Fuel* **2023**, *332*, 126106. https://doi.org/10.1016/j.fuel.2022.126106.
48. Huang, T.; Liang, T.; You, J.; et al. Coordination environment-tailored electronic structure of single atomic copper sites for efficient electrochemical nitrate reduction toward ammonia. *Energy Environ. Sci.* **2024**, *17*, 8360–8367. https://doi.org/10.1039/D4EE02746A.
49. Li, Y.; Lu, Z.; Zheng, L.; et al. The synergistic catalysis effect on electrochemical nitrate reduction at the dual-function active sites of the heterostructure. *Energy Environ. Sci.* **2024**, *17*, 4582–4593. https://doi.org/10.1039/D4EE00784K.
50. Yin, H.; Peng, Y.; Li, J. Electrocatalytic Reduction of Nitrate to Ammonia via a Au/Cu Single Atom Alloy Catalyst. *Environ. Sci. Technol.* **2023**, *57*, 3134–3144. https://doi.org/10.1021/acs.est.2c07968.
51. Du, C.; Lu, S.; Wang, J.; et al. Selectively Reducing Nitrate into NH3 in Neutral Media by PdCu Single-Atom Alloy Electrocatalysis. *ACS Catal.* **2023**, *13*, 10560–10569. https://doi.org/10.1021/acscatal.3c01088.
52. Cai, J.; Wei, Y.; Cao, A.; et al. Electrocatalytic nitrate-to-ammonia conversion with ~100% Faradaic efficiency via single-atom alloying. *Appl. Catal. B Environ.* **2022**, *316*, 121683. https://doi.org/10.1016/j.apcatb.2022.121683.
53. Yu, J.; Gao, R.T.; Guo, X.; et al. Electrochemical Nitrate Reduction to Ammonia on AuCu Single-Atom Alloy Aerogels under Wide Potential Window. *Angew. Chem. Int. Ed.* **2025**, *64*, e202415975. https://doi.org/10.1002/anie.202415975.
54. Suh, J.; Choi, H.; Kong, Y.; et al. Tandem Electroreduction of Nitrate to Ammonia Using a Cobalt–Copper Mixed Single-Atom/Cluster Catalyst with Synergistic Effects. *Adv. Sci.* **2024**, *11*, 2407250. https://doi.org/10.1002/advs.202407250.

55. Jiang, G.; Liu, Z.; He, S.; et al. Single-Atom Copper-Bearing Cerium Oxide Electrocatalysts Embedded in an Integrated System Enable Sustainable Nitrogen Recycling from Natural Water Bodies. *ACS EST Eng.* **2024**, *4*, 2912–2922. https://doi.org/10.1021/acsestengg.4c00299.
56. Liu, Z.; Shen, F.; Shi, L.; et al. Electronic Structure Optimization and Proton-Transfer Enhancement on Titanium Oxide-Supported Copper Nanoparticles for Enhanced Nitrogen Recycling from Nitrate-Contaminated Water. *Environ. Sci. Technol.* **2023**, *57*, 10117–10126. https://doi.org/10.1021/acs.est.3c03431.
57. Fang, L.; Wang, S.; Lu, S.; et al. Efficient electroreduction of nitrate via enriched active phases on copper-cobalt oxides. *Chin. Chem. Lett.* **2024**, *35*, 108864. https://doi.org/10.1016/j.cclet.2023.108864.
58. Wang, J.; Wang, Y.; Cai, C.; et al. Cu-Doped Iron Oxide for the Efficient Electrocatalytic Nitrate Reduction Reaction. *Nano Lett.* **2023**, *23*, 1897–1903. https://doi.org/10.1021/acs.nanolett.2c04949.
59. Zhou, B.; Tong, Y.; Yao, Y.; et al. Reversed I1Cu_4 single-atom sites for superior neutral ammonia electrosynthesis with nitrate. *Proc. Natl. Acad. Sci. USA* **2024**, *121*, e2405236121. https://doi.org/10.1073/pnas.2405236121.
60. Shi, L.; Li, Y.; He, S.; et al. Efficient electrocatalytic nitrate reduction on molecular catalyst with electron-deficient single-atom $Cu\delta^+$ sites. *Chem. Eng. J.* **2024**, *495*, 153427. https://doi.org/10.1016/j.cej.2024.153427.
61. Wang, Y.; Xia, S.; Zhang, J.; et al. Halogen-induced planar defects in Cu catalysts for ammonia electrosynthesis at an ampere-level current density. *Mater. Chem. Front.* **2023**, *7*, 3093–3101. https://doi.org/10.1039/D3QM00114H.